

# Cooperation among N, F and Fe in tri-doped TiO<sub>2</sub> photocatalyst

Yufei Zhang<sup>1</sup> · Huiyuan Shen<sup>1</sup> · Yanhua Liu<sup>1</sup>

Received: 18 September 2015 / Accepted: 22 January 2016 / Published online: 5 March 2016  
© Springer Science+Business Media Dordrecht 2016

**Abstract** TiO<sub>2</sub> photocatalysts tri-doped with N, F and Fe were synthesized by a sol–gel method. The cooperation of N, F and Fe in tri-doped TiO<sub>2</sub> was verified by monitoring NH<sub>3</sub> decomposition, X-ray diffraction (XRD), scanning electron microscopy (SEM), high-resolution transmission electron microscopy (HRTEM), X-ray photoelectron spectroscopy (XPS) and ultraviolet–visible (UV–Vis) absorption spectroscopy, and by the simulation based on the density functional theory (DFT). The results from NH<sub>3</sub> decomposition revealed that the cooperation of N, F and Fe broadened the optical response of TiO<sub>2</sub> to the visible light range and also enhanced the photocatalytic activity of TiO<sub>2</sub> under UV light. The reusability of the tri-doped TiO<sub>2</sub> sample after three cycles under UV and visible light irradiation was very good. XRD patterns and SEM and HRTEM images indicated that the tri-doped sample was nanometric anatase with a small amount of rutile with an average particle size of 18 nm. Tri-doping with N, F and Fe suppressed the phase transition from anatase to rutile and also resulted in some more lattice defects. XPS analysis showed that the N, F and Fe atoms were doped into the TiO<sub>2</sub> lattice. UV–Vis absorption spectra of the tri-doped TiO<sub>2</sub> showed that its optical absorption edge was moved up to 640 nm and its UV absorption was also enhanced. The DFT results confirmed that the cooperation of Fe 3d and N 2p orbits narrowed the band gap of TiO<sub>2</sub> and the F 2p orbit broadened the upper valence bands. The synergistic electron density around N, F and Fe in tri-doped TiO<sub>2</sub> was capable of enhancing the photochemical stability and reusability of TiO<sub>2</sub>.

**Keywords** Cooperation of N, F and Fe · Tri-doped TiO<sub>2</sub> · Light response performance · Photocatalytic activity · Density functional theory

---

✉ Yanhua Liu  
yhliu@mail.xjtu.edu.cn

<sup>1</sup> Department of Building Environment and Services Engineering, School of Human Settlements and Civil Engineering, Xi'an Jiaotong University, Xi'an 710049, China

## Introduction

Photocatalytic oxidation is a promising air-cleaning technology in decomposition of volatile organic compounds (VOCs) and mineralization of undesired chemical substances in indoor or outdoor air. Anatase TiO<sub>2</sub> is one of favorable photocatalysts due to its outstanding properties, such as nontoxicity, chemical inertness and stability over a wide pH range under irradiation conditions [1–5]. However, the removal efficiency is limited under solar radiation. This is because of the wide band gap of 3.2 eV for anatase TiO<sub>2</sub>, which can only exploit UV light ( $\lambda = 4 \times 10^{-3}$ –0.38  $\mu\text{m}$ ), accounting for only approximately 8.7 % of sunlight. The proportion of visible light ( $\lambda = 0.38$ –0.76  $\mu\text{m}$ ) is 44.6 %. Therefore, expanding the spectral response of anatase TiO<sub>2</sub> to the visible light region is attracting the attention of researchers. Elemental doping provides the possibility of broadening the spectral response range of anatase TiO<sub>2</sub>.

Metal and nonmetal elements were often used as doping elements. N doping has been demonstrated to be beneficial in extending the optical absorption edge of anatase TiO<sub>2</sub> [6–16]. Asahi et al. [6] reported that N doping improved photocatalytic activity under visible light irradiation by narrowing the band gap of anatase TiO<sub>2</sub>. It has been found that the localized N 2p states in anatase TiO<sub>2</sub> doped with N contributed to narrowing the band gap [7–9]. Fe ions are regarded as appropriate candidates because of the similar ionic radii of Fe<sup>3+</sup> (0.64 Å) and Ti<sup>4+</sup> (0.68 Å) [17]. It has been confirmed that Fe<sup>3+</sup> ions in Fe-doped anatase TiO<sub>2</sub> capture photogenerated electrons because the energy level of Fe<sup>3+</sup> is below the conduction band minimum (CBM). The ions also capture photogenerated holes because the energy level of Fe<sup>3+</sup> is above the valence band maximum (VBM) edge [18–22]. Fe doping is, therefore, believed to inhibit the recombination of photogenerated hole–electron pairs and improve the photocatalytic efficiency of anatase TiO<sub>2</sub>. In addition, F doping of anatase TiO<sub>2</sub> has been generally carried out in nonmetal and metal element co-doping [23–27].

Single dopings with N, F or Fe have their own merits. Co-doping or tri-doping with the nonmetal and metal elements is an attractive approach. It has been found that co-doping of nonmetal and metal elements is capable of extending the light absorption edge of TiO<sub>2</sub> to the visible light region [28–35]. Our previous research found that the co-doping of N and Fe ions played a more prominent role in improving photocatalytic activity of TiO<sub>2</sub> under visible light, and the co-doping of F and Fe ions is more beneficial to improving photocatalytic activity under UV light [36]. Thus, it is necessary to combine the respective advantages of the co-doping of N and Fe ions, and F and Fe ions. Nevertheless, past study on tri-doping is rare [37, 38] and synergistic effects of the tri-doping ions on photocatalytic activity have not been reported. Persuasive analysis based on the density functional theory (DFT) simulation and the degradation of gaseous pollutants has not been attempted. In this paper, a series of TiO<sub>2</sub> samples tri-doped with N, F and Fe were prepared by a sol–gel method. Their photocatalytic activity was evaluated by the decomposition of NH<sub>3</sub>. The cooperation of N, F and Fe in tri-doped TiO<sub>2</sub> was studied by use of X-ray diffraction (XRD), scanning electron microscopy (SEM), high-resolution

transmission electron microscopy (HRTEM), selected-area electron diffraction (SAED), X-ray photoelectron spectroscopy (XPS), ultraviolet–visible (UV–Vis) absorption spectroscopy, and simulation based on DFT.

## Experiments and simulation

### TiO<sub>2</sub> catalyst preparation

The Taguchi method is a powerful technique for the design of high-quality systems. In the work discussed in this paper, the conditions used for tri-doping of TiO<sub>2</sub> with N, F and Fe were selected by using the orthogonal array of the Taguchi quality design. The choosing of the range and values of concentration for the tri-doping N, F and Fe ions was based on our previous research [36]. The factors chosen and their levels are listed in Table 1. The samples prepared and the conditions used are listed in Table 2. For comparison, undoped TiO<sub>2</sub> samples were prepared at 400, 500 and 600 °C.

Undoped TiO<sub>2</sub> and TiO<sub>2</sub> tri-doped with N, F and Fe photocatalysts were prepared from Ti(OC<sub>4</sub>H<sub>9</sub>)<sub>4</sub> by use of a stepwise sol–gel method. The N used to dope the TiO<sub>2</sub> was from CO(NH<sub>2</sub>)<sub>2</sub>, the F was from NaF and the Fe was from Fe(NO<sub>3</sub>)<sub>3</sub>·9H<sub>2</sub>O. Hybrid sols were prepared by mixing these compounds with Ti(OC<sub>4</sub>H<sub>9</sub>)<sub>4</sub>, de-ionized water, and absolute ethyl alcohol. First, solution A was prepared by mixing 17 mL of Ti(OC<sub>4</sub>H<sub>9</sub>)<sub>4</sub> with 30 mL of absolute ethyl alcohol and stirring for 30 min. Solution B was then prepared by mixing 28.32 mL of absolute ethyl alcohol, 7.2 mL of de-ionized water, 20 mL of glacial acetic acid and the appropriate

**Table 1** Factors and levels

Control factor	Level 1	Level 2	Level 3
Doping amount of N (at%)	1	4	7
Doping amount of F (at%)	1	5	9
Doping amount of Fe (at%)	0.03	0.06	0.09
Calcination temperature	400	500	600

**Table 2** Samples prepared by tri-doping with N, F and Fe and the preparation conditions

Sample no.	F (at%)	Fe (at%)	Temp. (°C)	N (at%)
1	1	0.03	400	1
2	1	0.06	500	4
3	1	0.09	600	7
4	5	0.03	500	7
5	5	0.06	600	1
6	5	0.09	400	4
7	9	0.03	600	4
8	9	0.06	400	7
9	9	0.09	500	1

amount of  $\text{CO}(\text{NH}_2)_2$ , NaF and/or  $\text{Fe}(\text{NO}_3)_3 \cdot 9\text{H}_2\text{O}$ . Solution B was added to solution A and the mixture was stirred for 30 min to obtain a uniformly transparent sol. After aging of the sol for 24 h, a wet gel was obtained. The wet gel was placed in a drying cabinet at  $100^\circ\text{C}$ , set in advance, and removed when all the solvents had been completely volatilized. The dried gel was ground into powder, and the powder was calcined in a muffle furnace at a specific temperature for 2.5 h. Finally, nano- $\text{TiO}_2$  particles were prepared. The nano- $\text{TiO}_2$  particles were then applied as a coating on flat reactors. First, a nano- $\text{TiO}_2$  suspension liquid was prepared by adding the nano- $\text{TiO}_2$  particles to de-ionized water and stirring for 30 min. Glass slides were carefully cleaned with absolute ethyl alcohol, oven dried at  $100^\circ\text{C}$  for 1 h, dipped into the nano- $\text{TiO}_2$  suspension liquid for 1 h, then withdrawn at  $2.5\text{ cm min}^{-1}$ . The coated slides were then heated at  $150^\circ\text{C}$  for 3 h to furnish nano- $\text{TiO}_2$ -coated glass slides.

### Photocatalytic reaction

To evaluate the photocatalytic activity of  $\text{TiO}_2$  tri-doped with N, F and Fe, decomposition of  $\text{NH}_3$  was investigated by use of the  $\text{NH}_3$  generator and batch-type photocatalytic reaction system shown in Fig. 1.

The reaction system comprised a chamber, a fan, a Gasetm FTIR analyzer and valves connected by glass tubes. A flat photocatalytic reactor and a light source were present in the chamber. In the flat photocatalytic reactor the nano- $\text{TiO}_2$  coating was sealed under a quartz plate glass cover of area  $150\text{ cm}^2$ . In each run,  $0.635\text{ g}$  of  $\text{TiO}_2$  and  $3500\text{ mL}$  of reactant gas were sealed in the reactor loop. The light source was an incandescent lamp or a UV lamp, as shown in Fig. 1. The wavelength range of the incandescent lamp ( $60\text{ W}$ ) was from  $380$  to  $780\text{ nm}$  (Fig. 2). Its average intensity on the  $\text{TiO}_2$  was  $1060.8\text{ }\mu\text{W cm}^{-2}$ . The wavelength of the UV lamp ( $20\text{ W}$ ) was  $254\text{ nm}$ . Its average intensity on the  $\text{TiO}_2$  was  $1163\text{ }\mu\text{W cm}^{-2}$ . Compressed air from cylinder 1 was passed through the ammonia solution and carried  $\text{NH}_3$  into the reactor. The concentration of  $\text{NH}_3$  was regulated by changing

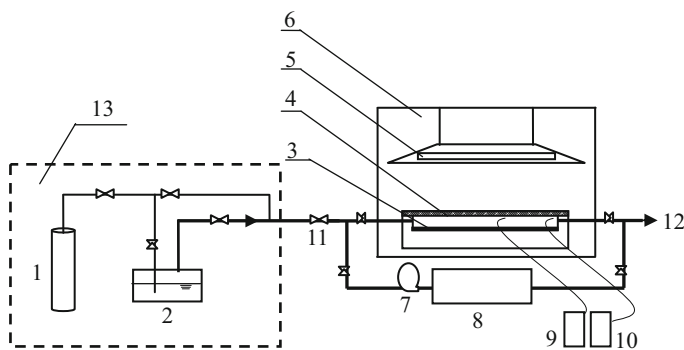


**Fig. 1** Experimental setup. 1 Cylinder air, 2  $\text{NH}_3$  solution, 3  $\text{TiO}_2$  coating, 4 flat photocatalytic reactor, 5 lamp (incandescent or UV), 6 reaction chamber, 7 fan, 8 Fourier transform infrared (FTIR) analyzer, 9 luminometer, 10 Testo 605-H1, 11 gas inlet, 12 gas outlet, 13  $\text{NH}_3$  generator

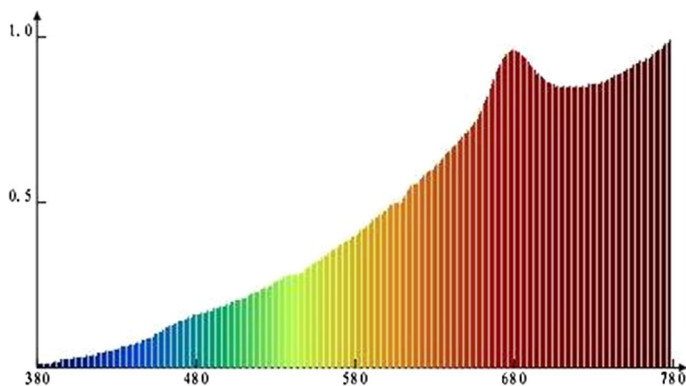


**Fig. 2** Wavelength distribution of the incandescent lamp (60 W)

the gas flow rate and the time the air was bubbled through the NH<sub>3</sub> solution. When NH<sub>3</sub> concentration in the system reached the value expected, the NH<sub>3</sub> generator was isolated from the reaction system. The reactant gas was then circulated in its loop. When the NH<sub>3</sub> concentration in the loop was steady, the lamp was turned on and the photocatalytic reaction started. The initial concentration in all experiments was  $155 \pm 4 \text{ mg m}^{-3}$ . The reaction time in each run was 45 min, the temperature  $25 \text{ }^\circ\text{C}$ , and the relative humidity  $55.6 \pm 3 \%$ . Before each run, the system was cleaned by purging with dried nitrogen gas until no NH<sub>3</sub> could be detected.

The concentration of NH<sub>3</sub> was measured by use of a Gaset FTIR analyzer, the uncertainty of which was  $\pm 2 \%$ . The error in NH<sub>3</sub> measurement was  $0.63 \%$ . Temperature and humidity were measured by use of a measurement stick (Testo 605-H1); uncertainties were  $\pm 0.5 \%$  for temperature and  $\pm 3 \%$  for humidity. Light intensity was measured by use of a Testo 545 with distinguishability of 1 Lux.

### Data processing

The concentration of NH<sub>3</sub> in the reaction system in Fig. 1 decreased as a function of time during each run. The decomposition ratio,  $R$ , for NH<sub>3</sub> on TiO<sub>2</sub> was calculated by use of the equation:

$$R = \frac{C_0 - C_e}{C_0} \times 100 \% \quad (1)$$

where  $C_0$  ( $\text{mg m}^{-3}$ ) was the initial concentration of NH<sub>3</sub> in the system and  $C_e$  ( $\text{mg m}^{-3}$ ) was the concentration of NH<sub>3</sub> at the end of a photocatalysis experiment (45 min).

### Characterization of TiO<sub>2</sub> samples

XRD with Cu-K $\alpha$  radiation (40 kV, 35 mA and  $\lambda = 0.154 \text{ nm}$ ) was used to determine the crystal structure of TiO<sub>2</sub> samples. UV-Vis absorption spectra of the solid samples were acquired in the range 240–2600 nm; the wavelength accuracy

was  $\pm 0.2$  nm. SEM of the samples was performed with a Joel JSM-7800F microscope with an operating voltage of 15 kV and a resolution of 0.8 nm. HRTEM images and SAED patterns of the samples were acquired by use of a Joel JEM-2100F with the field emission voltage of 200 kV and a lattice fringe resolution of 0.2 nm. XPS analysis of the samples was performed with a Kratos ULtrablend spectrometer with a monochromatic Al radiation source and best resolution of 0.48 eV.

### Simulation methodology

Simulation based on Kohn–Sham density functional theory (DFT) was performed by use of the Cambridge Sequential Total Energy Package (CASTEP). Twenty-four-atom  $2 \times 1 \times 1$  supercell models of undoped anatase  $\text{TiO}_2$ , anatase  $\text{TiO}_2$  doped with N, anatase  $\text{TiO}_2$  doped with F, anatase  $\text{TiO}_2$  doped with Fe, and anatase  $\text{TiO}_2$  doped with N, F and Fe were built. Figure 3 shows the perspective view of the 24-atom  $2 \times 1 \times 1$  supercell models.

The substitutional N doping was carried out by replacing an O atom with a N atom in the 24-atom  $2 \times 1 \times 1$  supercell model of doped  $\text{TiO}_2$  with N as shown in Fig. 3b. The substitutional F doping was carried out by replacing an O atom with a F atom in the 24-atom  $2 \times 1 \times 1$  supercell model of doped  $\text{TiO}_2$  with F as shown in

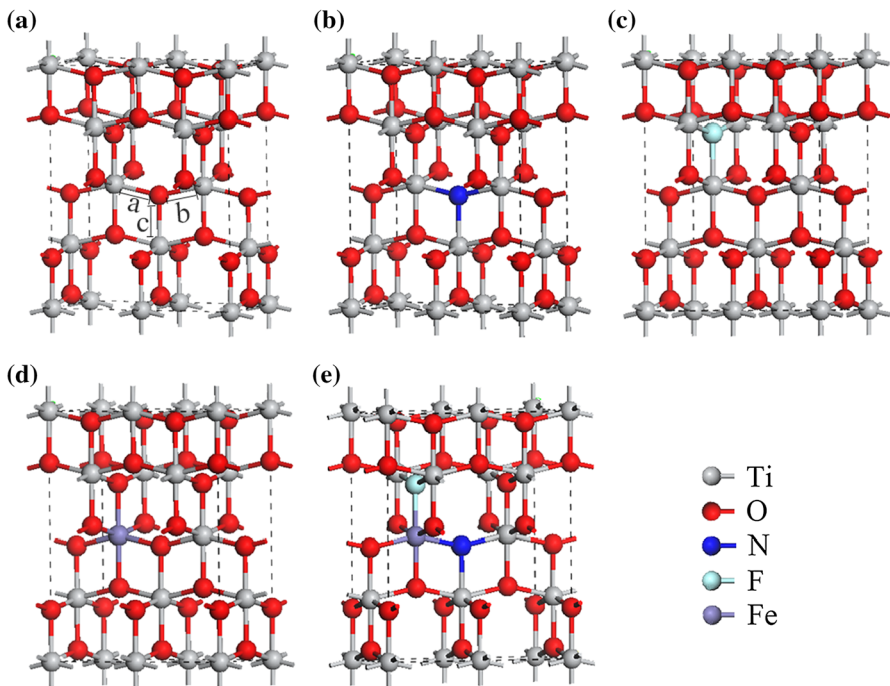


**Fig. 3** Perspective view of the 24-atom  $2 \times 1 \times 1$  supercell models of  $\text{TiO}_2$ . **a** Undoped  $\text{TiO}_2$ , **b** doped  $\text{TiO}_2$  with N, **c** doped  $\text{TiO}_2$  with F, **d** doped  $\text{TiO}_2$  with Fe, **e** tri-doped  $\text{TiO}_2$  with N, F and Fe

Fig. 3c. The substitutional Fe doping was carried out by replacing a Ti atom with a Fe atom in the 24-atom  $2 \times 1 \times 1$  supercell model of doped TiO<sub>2</sub> with Fe as shown in Fig. 3d. The substitutional N, F and Fe tri-doping was carried out by replacing an O atom with an N atom, by replacing a Ti atom near the N atom with an Fe atom and by replacing an O atom near the Fe atom with an F atom in the 24-atom  $2 \times 1 \times 1$  supercell model of tri-doped TiO<sub>2</sub> with N, F and Fe as shown in Fig. 3e. The doping concentration of N, F and Fe atoms was 4 at%. The cutoff energy for the plane wave was 400 eV and the Monkhorst–Pack  $k$ -point was generated with a  $3 \times 5 \times 2$  supercell grid. The cell parameters and the atomic positions of all structures were optimized till the residual force of all components was less than 0.025 eV/Å. The parameters were  $a = b = 3.78$  Å,  $c = 9.48$  Å as shown in Fig. 3a, consistent with the experimental results in Ref. [39]. The accurate density of states (DOS) was obtained by the self-consistent calculation and the convergence factor for the self-consistent energy set to  $2 \times 10^{-6}$  eV. After optimization of the supercell structures of undoped TiO<sub>2</sub>, TiO<sub>2</sub> doped with N, TiO<sub>2</sub> doped with F, TiO<sub>2</sub> doped with Fe, and TiO<sub>2</sub> tri-doped with N, F and Fe, their total density of states (TDOS), partial density of states (PDOS), and electron density difference (EDD) were calculated by use of the Kohn–Sham self-consistent equations, as follows:

$$\left[ \frac{-\hbar^2}{2m} \nabla^2 + V_{\text{ks}}[\rho(r)] \right] \Phi_i(\rho) = E_i \Phi_i(\rho) \quad (2)$$

$$V_{\text{ks}}[\rho(r)] = V_c(r) + V_{\text{ext}}(r) + V_{\text{xc}}(r) \quad (3)$$

$$V_c(r) = \int d^3r' \rho(r') \frac{e^2}{|r - r'|} \quad (4)$$

$$V_{\text{xc}}(r) = \frac{\delta E_{\text{xc}}[\rho(r)]}{\delta \rho(r)} \quad (5)$$

$$\rho(r) = \sum_i |\Phi_i(r)|^2 \quad (6)$$

where  $\hbar$  is Planck's constant (J s),  $m$  is the mass of an electron (kg),  $\nabla$  is the Laplace operator,  $r$  represents the position of an electron at any time,  $\rho(r)$  represents the electron density function of the ground state (a.u.),  $V_{\text{ks}}[\rho(r)]$  is the Kohn–Sham potential energy function (eV),  $\Phi(r)$  is the single-electron wave function,  $V_c(r)$  is the Coulomb repulsion potential function (eV),  $V_{\text{ext}}(r)$  contains the Coulomb attraction potential (eV) between the core and electron and the reaction potential of the external field,  $V_{\text{xc}}(r)$  are the exchange–correlation potentials (eV),  $E_{\text{xc}}[\rho(r)]$  is the exchange–correlation energy functional (eV) and is provided by the generalized gradient approximation (GGA) by Perdew, Burke and Ernzerhof (PBE) [40] as follows,

$$E_{\text{xc}}^{\text{GGA}}[\rho(r)] = \int \rho(r) \varepsilon_{\text{xc}}[\rho(r), \nabla \rho(r)] dr \quad (7)$$

where

$$\nabla\rho(r) = \rho(r) + d\rho(r) \quad (8)$$

and  $\varepsilon_{xc}[\rho(r), \nabla\rho(r)]$  is the exchange–correlation energy density of electron gas.

The TDOS is  $\rho(r)$  at each energy state point. The PDOS is  $\rho(r)$  at the energy state point of one electronic sub-layer. EDD is the  $\rho(r)$  difference of one atom after and before chemical binding.  $\rho(r)$  is calculated by iterative solution of the Kohn–Sham self-consistent equations. Therefore, TDOS, PDOS and EDD are solved. The single-electron wave function  $\Phi_i(r)$  is expanded by the plane wave function. To reduce the number of the plane wave basis, the reaction between the ionic entity and the valence electrons is characterized by the pseudo-potentials. The ionic entity includes inner electrons and the atomic nucleus. Therefore,  $V_c(r)$  is provided by the ultrasoft pseudo-potentials as follows:

$$V_c(r) = V_{\text{uspp}}(r) \quad (9)$$

where  $V_{\text{uspp}}(r)$  of Ti, O, N, F and Fe atoms is 310, 340, 250, 330 and 300 eV, respectively, and the plane wave function is:

$$\Phi_i(r) = \frac{1}{\sqrt{N\Omega}} \sum_G \mu(G) \exp[i(k + G) \cdot r] \quad (10)$$

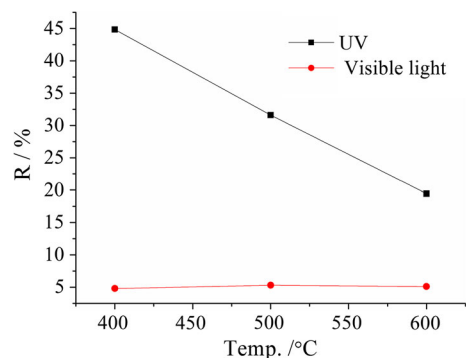
where  $N$  is the amount of original cell;  $\Omega$  is the volume of original cell ( $\text{nm}^3$ );  $\mu(G)$  is the expansion coefficient (m/k);  $k$  is the electron wave vector;  $G$  is the reciprocal lattice vector.

## Results and discussion

### Decomposition ratio of $\text{NH}_3$

The decomposition ratio of  $\text{NH}_3$  can be used to directly reflect the photocatalytic activity of the  $\text{TiO}_2$  samples. Figure 4 shows the decomposition ratio for  $\text{NH}_3$  on undoped  $\text{TiO}_2$  samples under the UV and incandescent lamps.

**Fig. 4** Decomposition ratio of  $\text{NH}_3$  on undoped  $\text{TiO}_2$  prepared at different calcination temperatures





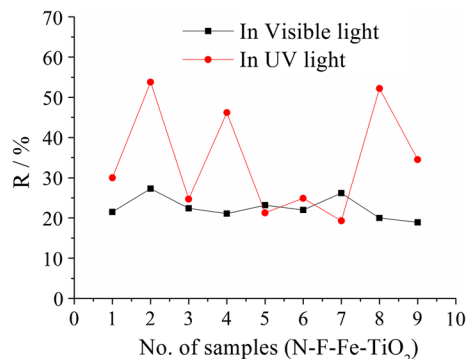
It is clear that under UV light, all the undoped TiO<sub>2</sub> samples had photocatalytic activity in the decomposition of NH<sub>3</sub>. Undoped TiO<sub>2</sub> prepared at 400 °C had the best photocatalytic activity; the decomposition ratio was approximately 45 %. With increasing calcination temperature the decomposition ratio for NH<sub>3</sub> in 45 min decreased. The decomposition ratio for undoped TiO<sub>2</sub> prepared at 600 °C was only approximately 19 %, indicating that a high calcination temperature is harmful to the photocatalytic activity of TiO<sub>2</sub>. Under the incandescent lamp, only approximately 5 % decomposition was achieved (Fig. 4). The ratio was close to that obtained when no TiO<sub>2</sub> was present in the system and is regarded as the result of photolysis. TiO<sub>2</sub> has no photocatalytic activity under visible light. The results indicate that use of undoped TiO<sub>2</sub> under visible light to purify outdoor air is infeasible.

In this work, TiO<sub>2</sub> samples tri-doped with N, F and Fe were prepared. The preparation conditions are listed in Table 2, including the amounts of N, F and Fe used for doping and the calcination temperature. Figure 5 shows the decomposition ratio for NH<sub>3</sub> on TiO<sub>2</sub> samples tri-doped with N, F and Fe.

It is clear that TiO<sub>2</sub> tri-doped with N, F and Fe has photocatalytic activity in NH<sub>3</sub> decomposition under visible light in Fig. 5. The results indicate that cooperation of the nonmetal N, F and the metal Fe can broaden the range of response of TiO<sub>2</sub> to visible light. The maximum of decomposition ratio among the samples reaches 28.1 % under visible light. Also, TiO<sub>2</sub> tri-doped with N, F and Fe has photocatalytic activity in NH<sub>3</sub> decomposition under UV light. The maximum decomposition ratio among the samples reaches 54.9 % under UV light, greater than that of undoped TiO<sub>2</sub>, indicating that the tri-doping with N, F and Fe also increases the activity of TiO<sub>2</sub> under UV light.

Figure 6 shows effects of N, Fe and F in tri-doped TiO<sub>2</sub> samples and calcination temperature on the decomposition ratio of NH<sub>3</sub> under visible and UV light. For the tri-doped TiO<sub>2</sub>, the composition ratio of NH<sub>3</sub> decreases a little bit firstly and then increases with the increasing of the amount of N, which means that ensuring a sufficient amount of N in the tri-doped TiO<sub>2</sub> is necessary for high-performance products. The quantitative change of F in the tri-doped TiO<sub>2</sub> samples has a little influence on NH<sub>3</sub> decomposition ratio. There is an optimal value for Fe element doping, which is 0.06 at% among the prepared samples. The effect of calcination temperature on NH<sub>3</sub> decomposition under visible light is weak.

**Fig. 5** Decomposition ratio of NH<sub>3</sub> on TiO<sub>2</sub> tri-doped with N, F and Fe



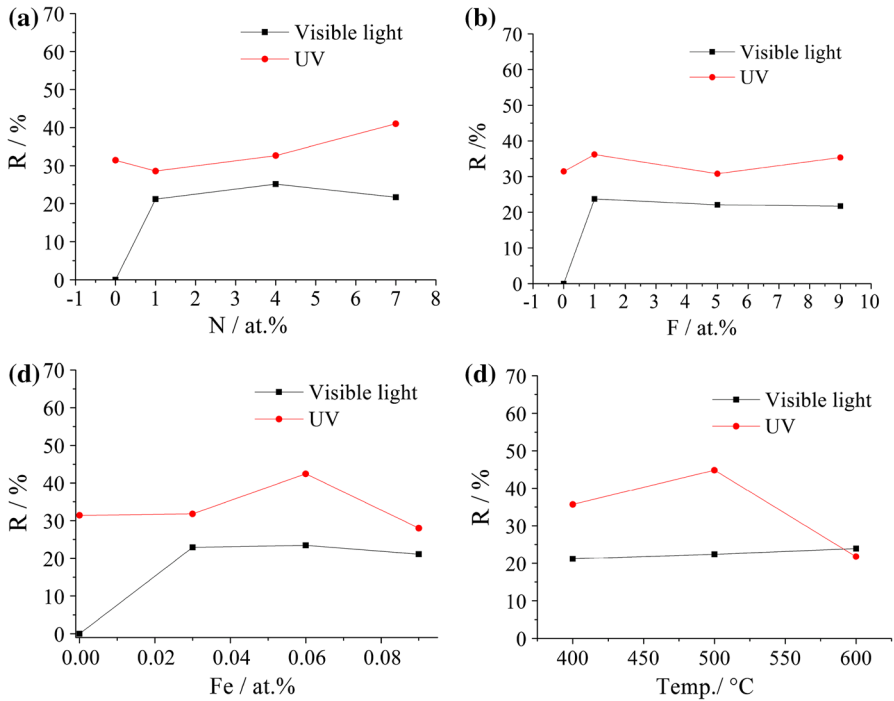


**Fig. 6** Effects of N, F, Fe and calcination temperature for  $\text{TiO}_2$  tri-doped with N, F and Fe

### Reusability of the tri-doped $\text{TiO}_2$ sample

The reusability of the tri-doped  $\text{TiO}_2$  sample is a key step for practical application of photocatalysis technology. An examination of the photocatalytic activity of the recycled tri-doped  $\text{TiO}_2$  sample was carried out under UV and visible light irradiation.

The results under UV light irradiation are shown in Fig. 7 and Table 3. The decomposition ratio of  $\text{NH}_3$  is still higher than 51.3 %, decreased by 0.8 % after three cycles. The results under visible light irradiation are shown in Fig. 8 and Table 3. The decomposition ratio of  $\text{NH}_3$  is still higher than 26.9 %, decreased by 0.4 % after three cycles. Therefore, the reusability of the tri-doped  $\text{TiO}_2$  sample under UV and visible light irradiation is very good.

### XRD patterns

Photocatalytic activities of  $\text{TiO}_2$  photocatalysts are affected by the phase transition and the changes of grain size, the lattice distortion and the crystallinity, obtained from XRD patterns. Figure 9 shows the XRD patterns of undoped  $\text{TiO}_2$  samples prepared at 400 °C, 500 °C and 600 °C and  $\text{TiO}_2$   $\text{N}(4\%)$  $\text{F}(9\%)$  $\text{Fe}(0.03\%)$  prepared at 600 °C with 4 at% N, 9 at% F and 0.03 at% Fe.

**Fig. 7** Reusability of the tri-doped TiO<sub>2</sub> sample for NH<sub>3</sub> decomposition under UV light irradiation

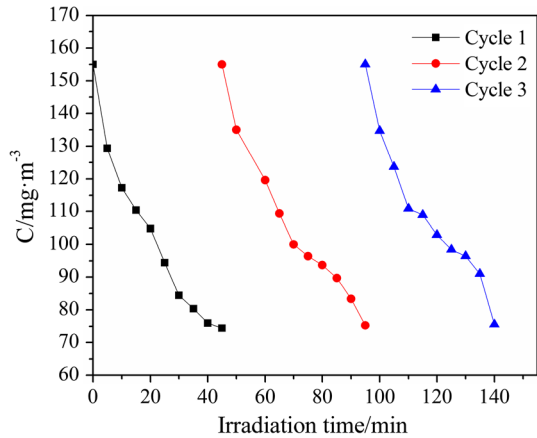
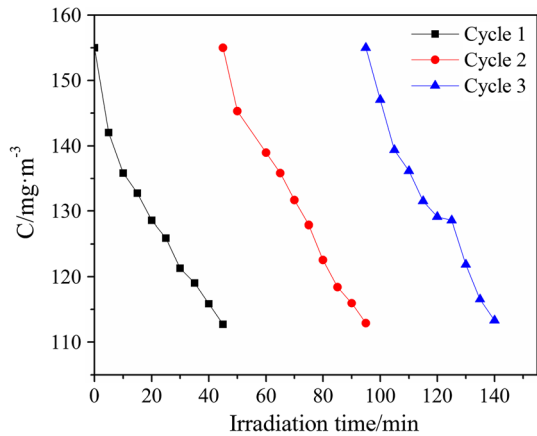


**Table 3** Data for the reusability photocatalytic experiments for the tri-doped TiO<sub>2</sub> sample under UV light irradiation

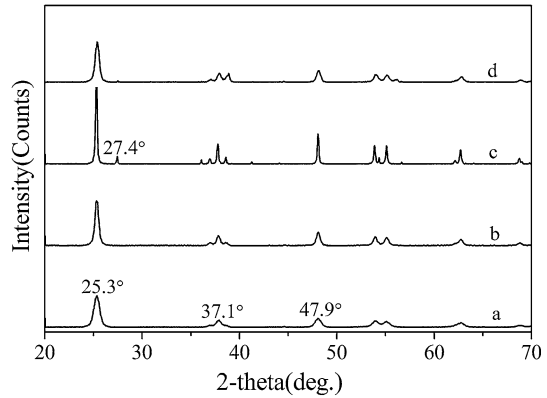
Type of light irradiation	Decomposition ratio of NH <sub>3</sub> (%)		
	Cycle 1	Cycle 2	Cycle 3
The tri-doped TiO <sub>2</sub> sample under UV light	52.1	51.5	51.3
The tri-doped TiO <sub>2</sub> sample under visible light	27.3	27.1	26.9

**Fig. 8** Reusability of the tri-doped TiO<sub>2</sub> sample for NH<sub>3</sub> decomposition under visible light irradiation



The diffraction peaks at  $2\theta = 25.3^\circ$ ,  $2\theta = 37.1^\circ$  and  $2\theta = 47.9^\circ$  indicate that all TiO<sub>2</sub> samples prepared are anatase except an undoped TiO<sub>2</sub> prepared at 600 °C. When the calcinated temperature is set at 600 °C, the diffraction peak at  $2\theta = 27.3^\circ$  appears, indicating that a part of TiO<sub>2</sub> is shifted to rutile. Rutile shows no photocatalytic activities. There is a very weak diffraction peak at  $2\theta = 27.3^\circ$  for

**Fig. 9** XRD patterns of undoped and tri-doped TiO<sub>2</sub> samples: *a* TiO<sub>2</sub> prepared at 400 °C, *b* TiO<sub>2</sub> prepared at 500 °C, *c* TiO<sub>2</sub> prepared at 600 °C, *d* TiO<sub>2</sub> N(4 % )F(9 % )Fe(0.03 %) prepared at 600 °C



TiO<sub>2</sub> N(4 % )F(9 % )Fe(0.03 %) prepared at 600 °C in Fig. 9d, indicating that tri-doping of N, F and Fe elements can lower the chance of TiO<sub>2</sub> to be shifted towards rutile.

The grain size is calculated by the Scherrer equation below:

$$D = \frac{K\lambda}{FW(S) * \cos \theta} \quad (11)$$

where  $D$  is the grain size (nm);  $K$  is a constant, generally 0.89;  $\lambda$  is the wave length of X-rays with 0.154 nm;  $FW(S)$  is the half height width of the diffraction peaks (rad.) and  $\theta$  is the diffraction angle (°). The lattice distortion is calculated by the formula below:

$$\varepsilon = \frac{\Delta D}{D} = \frac{FW(S)}{4 \tan(\theta)} \quad (12)$$

where  $\varepsilon$  is the lattice distortion (%);  $D$  is the average grain size (nm);  $FW(S)$  is the half height width of the diffraction peaks (rad.) and  $\theta$  is the diffraction angle (°).

On the basis of the XRD spectra in Fig. 9, grain size and lattice distortion were calculated for two samples, and the results are listed in Table 4. The results show that the samples prepared are nanoscale and have slight lattice distortion. The grain size of TiO<sub>2</sub> N(4 % )F(9 % )Fe(0.03 %) prepared at 600 °C is 16.26 nm, less than that (32.21 nm) of undoped TiO<sub>2</sub> prepared at 600 °C. The lattice distortion of TiO<sub>2</sub> N(4 % )F(9 % )Fe(0.03 %) prepared at 600 °C is 0.94 %, greater than that (0.31 %) of undoped TiO<sub>2</sub>. The results indicate that tri-doping with N, F and Fe inhibits grain growth of TiO<sub>2</sub> and results in a larger lattice distortion.

**Table 4** Grain size and lattice distortion of the samples prepared

Samples	$D$ (nm)	$\varepsilon$ (%)
TiO <sub>2</sub> N(4 % )F(9 % )Fe(0.03 %) prepared at 600 °C	16.26	0.94
Undoped TiO <sub>2</sub> prepared at 600 °C	32.21	0.31

## SEM images

Morphology and grain size of the samples were studied by SEM. Figure 10 shows SEM images of undoped TiO<sub>2</sub> prepared at 600 °C at different magnifications.

Figure 11 shows SEM images of TiO<sub>2</sub> N(4 %)F(9 %)Fe(0.03 %) prepared at 600 °C at different magnifications. The surface morphology of undoped TiO<sub>2</sub> particles prepared at 600 °C (Fig. 10a) is nubby, and is indicative of a random agglomeration structure, which arises from its nanoscale grain size, approximately 35 nm, as shown in Fig. 10b. Nevertheless, the morphology of TiO<sub>2</sub> N(4 %)F(9 %)Fe(0.03 %) particles prepared at 600 °C (Fig. 11a) are spherical and have better dispersion, and the grain size is approximately 18 nm (Fig. 11b). The main reasons for these changes may be synergistic effects of N, F and Fe tri-doping on the grain growth and crystal structure of anatase TiO<sub>2</sub>. All the results from SEM analysis are in good agreement with the results from XRD analysis in Fig. 9 and Table 4.

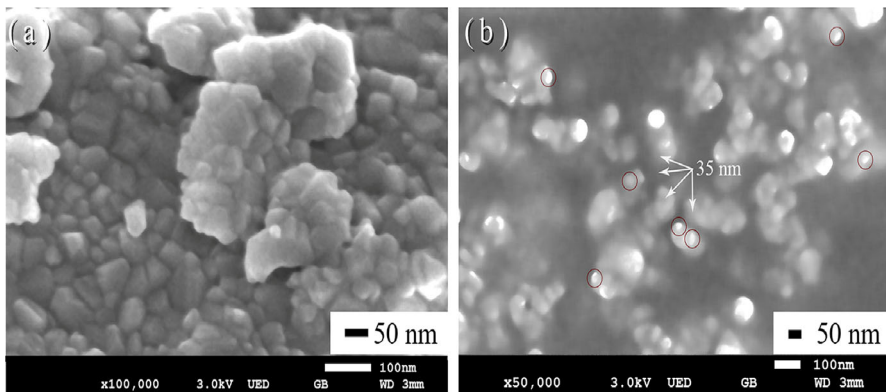


**Fig. 10** SEM images of undoped TiO<sub>2</sub> prepared at 600 °C at different magnifications

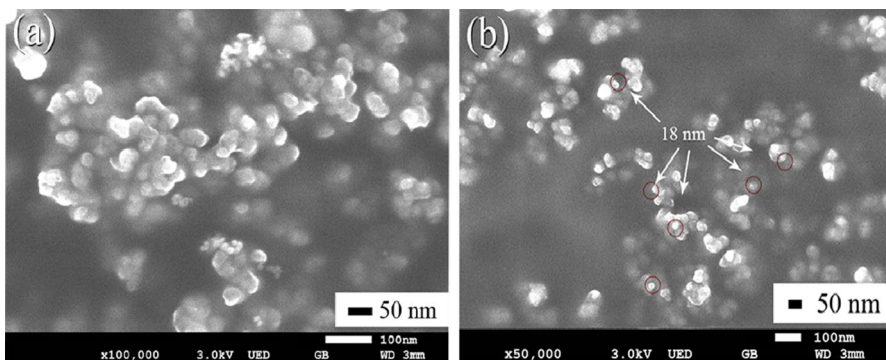


**Fig. 11** SEM images of TiO<sub>2</sub> N(4 %)F(9 %)Fe(0.03 %) prepared at 600 °C at different magnification

## HRTEM images and SAED patterns

The HRTEM images and SAED patterns of undoped  $\text{TiO}_2$  prepared at  $600\text{ }^\circ\text{C}$  and  $\text{TiO}_2_{\text{N}(4\%)\text{F}(9\%)\text{Fe}(0.03\%)}$  prepared at  $600\text{ }^\circ\text{C}$  are presented in Figs. 12 and 13, respectively.

It is clearly apparent that the particles of undoped  $\text{TiO}_2$  prepared at  $600\text{ }^\circ\text{C}$  are agglomerated and nubby in Fig. 12a. The particles seem to be nearly uniform in size, with an average size of 35 nm. Figure 12b shows the highly ordered crystalline planes of anatase (101) and (200), with fine fringe d-spacing of 0.35 and 0.19 nm, respectively, in the A area, and rutile (110), with fine fringe d-spacing of 0.33 nm in the B area. The SAED patterns of the A and B areas are shown in Fig. 12c, d. The SAED patterns contain bright points, which confirms the highly ordered structure of crystalline  $\text{TiO}_2$  nanoparticles. Figure 13a shows the nanoparticles of  $\text{TiO}_2_{\text{N}(4\%)\text{F}(9\%)\text{Fe}(0.03\%)}$  prepared at  $600\text{ }^\circ\text{C}$  are more dispersed and more spherical, with an average size of 18 nm, than those of undoped  $\text{TiO}_2$  prepared at  $600\text{ }^\circ\text{C}$ . Figure 13b shows the crystalline planes of anatase (101) with lattice fringe d-spacing of 0.35 nm, rutile (110) with lattice fringe d-spacing of 0.33 nm and large lattice fringe distortion. The SAED pattern in the inset Fig. 13b

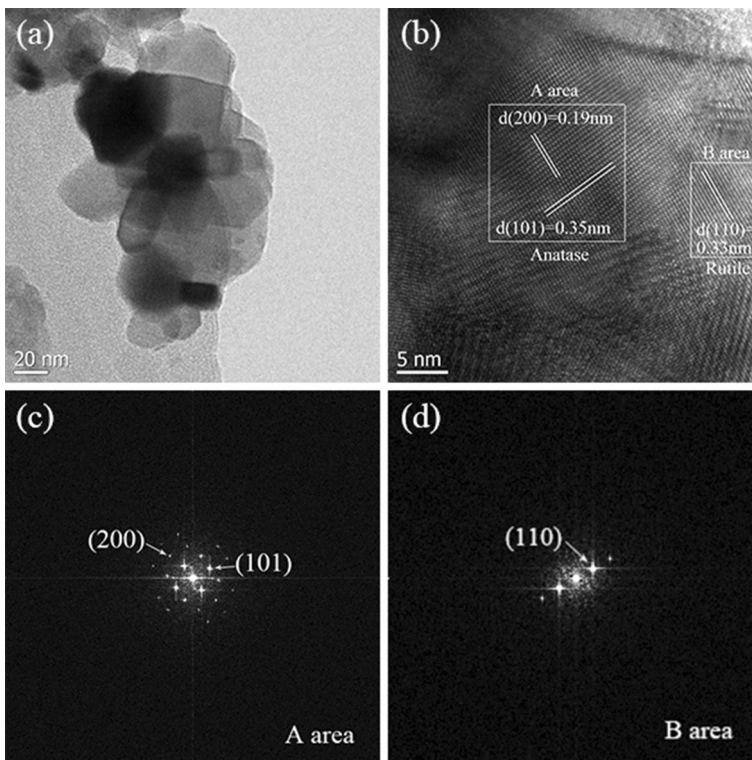


**Fig. 12** a, b HRTEM images at different magnification of undoped  $\text{TiO}_2$  prepared at  $600\text{ }^\circ\text{C}$ ; c, d SAED patterns of A area and B area in HRTEM images of undoped  $\text{TiO}_2$  prepared at  $600\text{ }^\circ\text{C}$

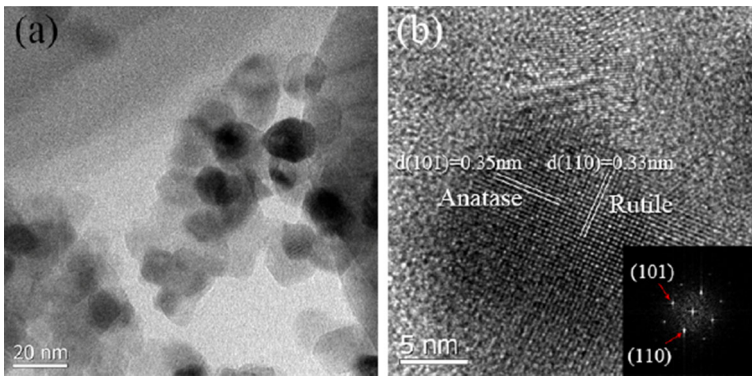


**Fig. 13** a, b HRTEM images at different magnification of TiO<sub>2</sub> N(4 %)F(9 %)Fe(0.03 %) prepared at 600 °C; the inset shows the SAED pattern

contains some unclear points which further confirms that the crystallinity of TiO<sub>2</sub> N(4 %)F(9 %)Fe(0.03 %) prepared at 600 °C is no better than that of undoped TiO<sub>2</sub> prepared at 600 °C, and that the TiO<sub>2</sub> N(4 %)F(9 %)Fe(0.03 %) prepared at 600 °C has some lattice defects. These results are very consistent with XRD patterns and SEM images.

### XPS analysis

To investigate the states of the tri-doped N, F and Fe, TiO<sub>2</sub> N(4 %)F(9 %)Fe(0.03 %) prepared at 600 °C was subjected to XPS analysis. Figure 14 shows the XPS survey spectrum and the high-resolution XPS spectra of TiO<sub>2</sub> N(4 %)F(9 %)Fe(0.03 %) prepared at 600 °C.

The XPS survey spectrum of TiO<sub>2</sub> N(4 %)F(9 %)Fe(0.03 %) prepared at 600 °C in Fig. 14a shows the presence of Ti 2p, O 1s, N 1s, F 1s and Fe 2p. The N 1s, F 1s and Fe 2p signals are weak, because of the small amounts of N, F and Fe. The signal of N 1s, especially, can be only obtained from the inset of Fig. 14a by magnifying the local area. The high-resolution XPS spectrum for Ti 2p in Fig. 14b contain two peaks at approximately 458.3 eV (Ti 2p<sub>3/2</sub>) and 464.1 eV (Ti 2p<sub>1/2</sub>), indicating that Ti is mainly present as Ti<sup>4+</sup>, on the basis of the literature [41, 42]. Figure 14c shows the high-resolution XPS spectrum for N 1s. Two peaks are observed at binding energies of approximately 398.5 and 401.2 eV. Previous work [41, 43] attributed the binding energy peak at 398.5 eV to an O–Ti–N structural feature formed by typical substitutional N doping of TiO<sub>2</sub>. The higher binding energy peak at 401.6 eV is assigned to the Ti–O–N linkage. However, this peak is less obvious and the intensity is weak, so we believe N atoms are mainly replacing lattice oxygen atoms in the doped TiO<sub>2</sub>. The high-resolution XPS spectrum for F 1s in Fig. 14d contains two peaks at approximately 683.3 eV and 686.5 eV. The F 1s peak located at 683.3 eV is ascribed to the fluorinated compounds adsorbed on the surface; The small F 1s peak located at 686.5 eV is originated from the substitutional F which occupies oxygen sites into the TiO<sub>2</sub> crystal lattice [37, 44]. The high-resolution XPS



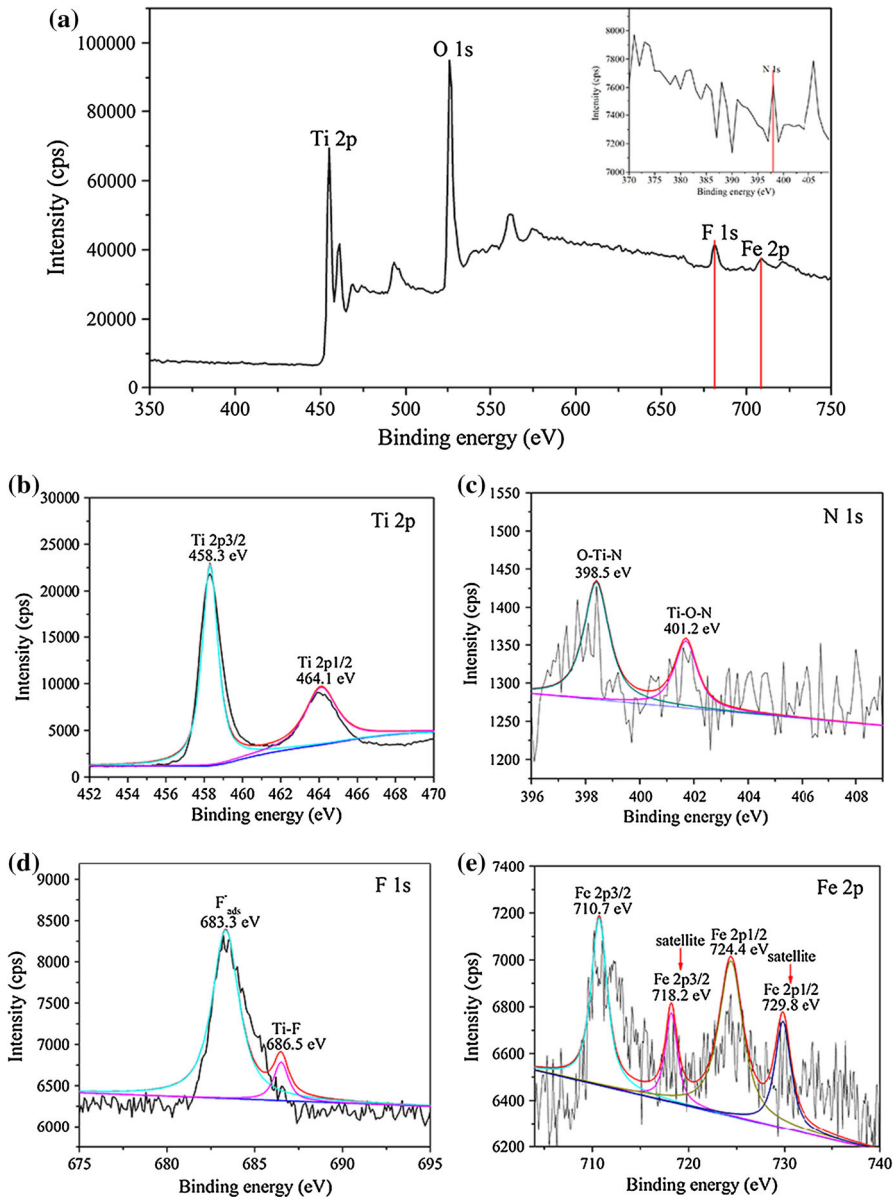


**Fig. 14** XPS survey spectra and high-resolution XPS spectra of  $\text{TiO}_2$   $\text{N}(4\%)\text{F}(9\%)\text{Fe}(0.03\%)$  prepared at  $600\text{ }^\circ\text{C}$ : **a** survey spectra, the inset shows the position of N 1s; **b** Ti 2p; **c** N 1s; **d** F 1s; **e** Fe 2p

spectrum for Fe 2p in Fig. 14e contains four peaks: a peak at a binding energy of 710.7 eV (Fe 2p<sub>3/2</sub>), a peak at about 724.4 eV (Fe 2p<sub>1/2</sub>), and the two other satellite peaks at binding energies of 718.2 eV (Fe 2p<sub>3/2</sub>) and 729.8 eV (Fe 2p<sub>1/2</sub>). These four characteristic peaks indicate that the doped Fe is in +3 state, which



confirms that Fe atoms are successfully replacing lattice Ti atoms in the doped TiO<sub>2</sub> [45]. The tri-dopants N, F and Fe are successfully replacing lattice oxygen atoms and Ti atoms, respectively, into the TiO<sub>2</sub> lattice.

### UV–Vis absorption spectra

The photocatalytic activity of TiO<sub>2</sub> is related to the range of its spectral response. Figure 15 shows UV–Vis absorption spectra of undoped samples prepared at 400, 500 and 600 °C, and TiO<sub>2</sub> N(4 %)F(9 %)Fe(0.03 %) sample prepared at 600 °C.

The three undoped TiO<sub>2</sub> samples almost had no response to visible light. Their absorbing edges are at around 416 nm. Surprisingly, after the modification, the light absorption edge of TiO<sub>2</sub> is extended to approximately 640 nm, i.e. the adsorption edge of TiO<sub>2</sub> is shifted to visible light region by the tri-doping. According to the energy formula below,

$$E_g = \frac{hc}{\lambda} \quad (13)$$

where  $\lambda$  is the wave length (nm),  $h$  is the Planck's constant (J s),  $c$  is the light speed (m/s), the energy gap value of TiO<sub>2</sub> N(4 %)F(9 %)Fe(0.03 %) sample prepared at 600 °C is approximately 1.9 eV. These results are consistent with those in Fig. 5, i.e. the cooperation of nonmetal N, F and metal Fe can broaden the light response range of TiO<sub>2</sub> to the visible light region. Moreover, the absorption ratio of UV light for tri-doped TiO<sub>2</sub> sample is higher than that of three undoped TiO<sub>2</sub> samples. The results demonstrate that the cooperation of N, F and Fe not only broadens the light response range of TiO<sub>2</sub>, but also enhances the absorption in the UV light region.

### Total density of states

The spectral response range of TiO<sub>2</sub> photocatalyst depends on its band structure. Figure 16 shows the TDOS of undoped TiO<sub>2</sub>, TiO<sub>2</sub> doped with N, TiO<sub>2</sub> doped with

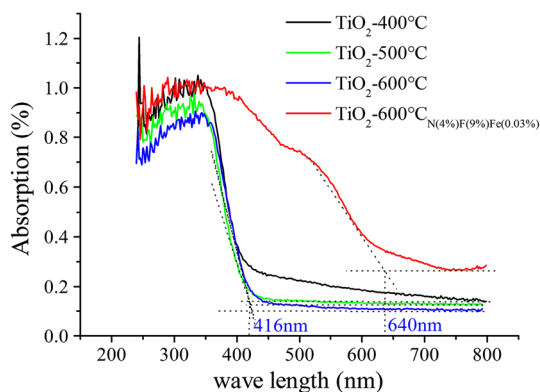


**Fig. 15** UV–Vis absorption spectra of undoped samples prepared at 400 °C, 500 °C and 600 °C, and TiO<sub>2</sub> N(4 %)F(9 %)Fe(0.03 %) sample prepared at 600 °C

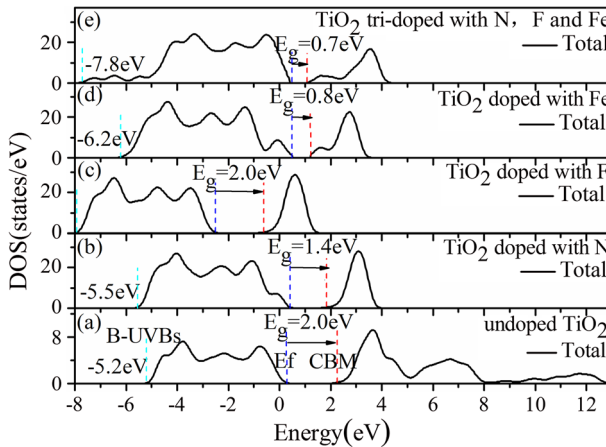


**Fig. 16** TDOS of *a* undoped TiO<sub>2</sub>, *b* TiO<sub>2</sub> doped with N, *c* TiO<sub>2</sub> doped with F, *d* TiO<sub>2</sub> doped with Fe, and *e* TiO<sub>2</sub> tri-doped with N, F and Fe

F, TiO<sub>2</sub> doped with Fe and TiO<sub>2</sub> tri-doped with N, F and Fe.  $E_g$  denotes the energy gap. The Fermi energy ( $E_f$ ) level is at the top of the valence band and is denoted with a black perpendicular dotted line. The red perpendicular dotted line on its right side marks the position of conduction band minimum (CBM). The cyan perpendicular dotted line on its left side marks the position of the bottom of upper valence bands (B-UVBs).

The calculated energy gap values of undoped TiO<sub>2</sub>, TiO<sub>2</sub> doped with N, TiO<sub>2</sub> doped with F, TiO<sub>2</sub> doped with Fe and TiO<sub>2</sub> tri-doped with N, F and Fe are 2.0, 1.4, 2.0, 0.8 and 0.7 eV, respectively. The results indicate that N doping, Fe doping and tri-doping with N, F and Fe can narrow the band gap of anatase TiO<sub>2</sub>, but F doping does not. The energy gap value of TiO<sub>2</sub> tri-doped with N, F and Fe is the smallest. Although the calculated energy gap value of undoped TiO<sub>2</sub> is 2.0 eV, smaller than the experimental value of 3.2 eV, this does not affect the reliability of the above conclusions. It is corrected by adding 1.2 eV to the calculated energy gap value [8]. Therefore, the calculated energy gap value of TiO<sub>2</sub> tri-doped with N, F and Fe should be corrected for 1.9 eV by adding 1.2 eV. This result is consistent with that in Fig. 15, i.e. according to Eq. (13) and the results in Fig. 16, N doping, Fe doping and tri-doping with N, F and Fe all expand the range of the spectral response of TiO<sub>2</sub> in the visible light region. The effectiveness is best for TiO<sub>2</sub> tri-doped with N, F and Fe.

In contrast with undoped TiO<sub>2</sub> in Fig. 16, the  $E_f$  levels of TiO<sub>2</sub> doped with N, TiO<sub>2</sub> doped with Fe and TiO<sub>2</sub> tri-doped with N, F and Fe move to higher energy levels, and their CBM moves to lower energy levels, which narrows the band gap of TiO<sub>2</sub>. Also, their B-UVBs levels move to lower energy levels, among which the B-UVB levels of tri-doped TiO<sub>2</sub> are the lowest, only -7.8 eV. This indicates that the width of the upper valence bands of TiO<sub>2</sub> tri-doped with N, F and Fe is the greatest. The upper valence bands are wider and the absorption of UV light is better.

Therefore, the tri-doping with N, F and Fe not only broadens the light response range of TiO<sub>2</sub>, but also enhances absorption in the UV light region.

### Partial density of states

The band structure in the TDOS is ascribed by the partial density of states (PDOS). Figure 17 shows PDOS and TDOS of TiO<sub>2</sub> tri-doped with N, F and Fe.

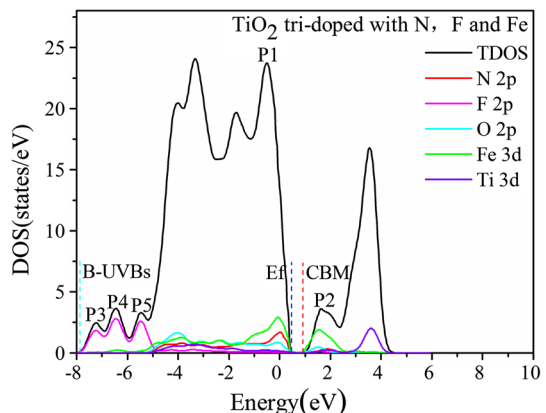
It is observed that the P1 peak of TiO<sub>2</sub> tri-doped with N, F and Fe is mainly contributed by Fe 3d and N 2p orbitals in Fig. 17, which raises the E<sub>f</sub> level to a higher energy level. The P2 peak of TiO<sub>2</sub> tri-doped with N, F and Fe is mainly contributed by Fe 3d orbit, which moves the CBM to a lower energy level. So, both P1 and P2 peaks contribute to narrowing the band gap. Moreover, three small P3, P4 and P5 peaks are contributed to by an F 2p orbit, which broadens the upper valence bands of TiO<sub>2</sub> and enhances the absorption performance in the UV light region.

In conclusion, the doping of N and Fe elements narrows the band gap of TiO<sub>2</sub>, and the doping of F element broadens the upper valence bands. The cooperation of N, F and Fe enhances both the light response performance of TiO<sub>2</sub> under UV and visible light. The results of TDOS and PDOS are consistent with that from UV–Vis absorption spectra analysis in Fig. 15, i.e. the tri-doping of N, F and Fe within TiO<sub>2</sub> is a good way to improve the light response performance of TiO<sub>2</sub>.

### Electron density difference

Electron density difference (EDD) can reflect electrons transfer around the atom and changes of charge density around the bond; this can aid further analysis of the covalent energy and photochemical stability of the TiO<sub>2</sub> molecule. Figure 18 shows the EDDs of undoped TiO<sub>2</sub>, TiO<sub>2</sub> doped with N, TiO<sub>2</sub> doped with F, TiO<sub>2</sub> doped with Fe and TiO<sub>2</sub> tri-doped with N, F and Fe. The red area where the EDD is negative indicates the loss of electrons, and the blue area where the EDD is positive indicates electron enrichment.

**Fig. 17** PDOS and TDOS of TiO<sub>2</sub> tri-doped with N, F and Fe



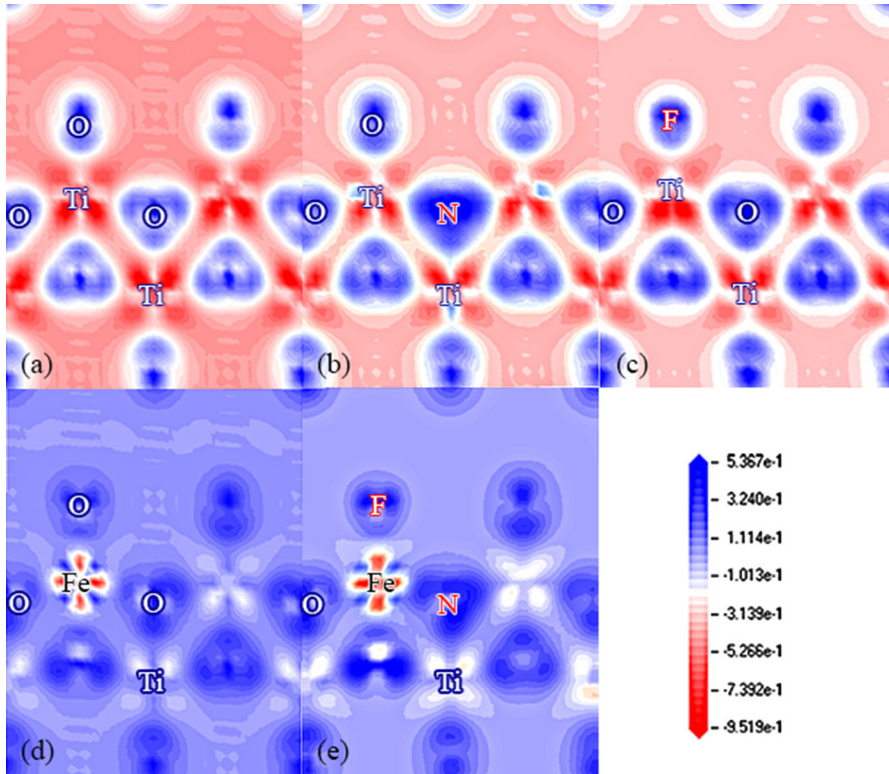


**Fig. 18** EDD plots of **a** undoped  $\text{TiO}_2$ , **b**  $\text{TiO}_2$  doped with N, **c**  $\text{TiO}_2$  doped with F, **d**  $\text{TiO}_2$  doped with Fe and **e**  $\text{TiO}_2$  tri-doped with N, F and Fe

In Fig. 18e, the size of the blue area around the F and N atoms in F–Fe–N–Ti links is larger and the color of the blue area is darker, compared with that at the same location in Fig. 18a, b, c. This demonstrates that the electron cloud of the F–Fe bond in F–Fe–N–Ti links of  $\text{TiO}_2$  tri-doped with N, F and Fe moves toward Fe, and the density of the electron cloud is greater than that of the O–Ti bonds of undoped  $\text{TiO}_2$  and  $\text{TiO}_2$  doped with N, and that of the F–Ti bond  $\text{TiO}_2$  doped with F at the same location; The electron cloud of the Fe–N bond in F–Fe–N–Ti links of  $\text{TiO}_2$  tri-doped with N, F and Fe moves toward Fe, and the density of the electron cloud is greater than that of the Ti–O bonds of undoped  $\text{TiO}_2$  and  $\text{TiO}_2$  doped with F, and that of the Ti–N bond of  $\text{TiO}_2$  doped with N at the same location; The electron cloud of the N–Ti bond in F–Fe–N–Ti links moves toward Ti of  $\text{TiO}_2$  tri-doped with N, F and Fe and the density of the electron cloud is greater than that of the O–Ti bonds of undoped  $\text{TiO}_2$  and  $\text{TiO}_2$  doped with F, and that of the N–Ti bond of  $\text{TiO}_2$  doped with N at the same location. Therefore, the covalent energy of the F–Fe, Fe–N and N–Ti bonds in F–Fe–N–Ti links of  $\text{TiO}_2$  tri-doped with N, F and Fe is higher than that of the bonds at the same location of undoped  $\text{TiO}_2$ ,  $\text{TiO}_2$  doped with

N and TiO<sub>2</sub> doped with F. Furthermore, in Fig. 18e, the size of the blue area around the O atom in O–Fe–N links is larger and the color of the blue area is darker, compared with that around the O atom in O–Ti–O and O–Ti–N links at the same location in Fig. 18a, b, c. This indicates that the electron cloud of the O–Fe bond in O–Fe–N links of tri-doped TiO<sub>2</sub> with N, F and Fe moves toward Fe and the density of the electron cloud is greater than that of the O–Ti bonds in O–Ti–O links of undoped TiO<sub>2</sub> and TiO<sub>2</sub> doped with F, and in O–Ti–N links of TiO<sub>2</sub> doped with N at the same location. Therefore, the covalent energy of the O–Fe bond in O–Fe–N links of TiO<sub>2</sub> tri-doped with N, F and Fe is higher than that of the O–Ti bonds in O–Ti–O links of undoped TiO<sub>2</sub> and TiO<sub>2</sub> doped with F, and in O–Ti–N links of TiO<sub>2</sub> doped with N at the same location. Anyway, the covalent energy of TiO<sub>2</sub> tri-doped with N, F and Fe is higher than that of undoped TiO<sub>2</sub>, TiO<sub>2</sub> doped with N and TiO<sub>2</sub> doped with F.

Additionally, in Fig. 18d, the blue area of TiO<sub>2</sub> doped with Fe tends to distribute around Fe, Ti and O, not among them. This indicates that the electron density around Fe, Ti and O significantly increases. Therefore, Fe doping increases the ionicity of TiO<sub>2</sub>, which is not conducive to the improvement of the photocatalytic activity of TiO<sub>2</sub>.

In summary, TiO<sub>2</sub> tri-doped with N, F and Fe has higher covalent energy than undoped and single-doped TiO<sub>2</sub>. The covalent energy of the photocatalyst is higher, its crystalline structure, especially its band structure, is more stable, the ability of resisting the corrosion of photochemical reactions is stronger and its photochemical stability is better. The above indicates that the photocatalytic activity of TiO<sub>2</sub> tri-doped with N, F and Fe under UV or visible light irradiation is very stable. These results are very consistent with those from Figs. 7, 8 and Table 3. Therefore, under synergistic action of the electron density around N, F and Fe in tri-doped TiO<sub>2</sub>, its photochemical stability and reusability are better than undoped and single-doped TiO<sub>2</sub>.

## Conclusions

1. NH<sub>3</sub> decomposition of undoped TiO<sub>2</sub> and TiO<sub>2</sub> samples tri-doped with N, F and Fe demonstrated that the cooperation of nonmetal N, F and metal Fe not only broadened the optical response range of TiO<sub>2</sub> to the visible light region, but also enhanced the activity of TiO<sub>2</sub> under UV light. The maximum decomposition ratio among the tri-doped samples under visible and UV light reached about 28.1 and 54.9 %, respectively. In the tri-doped TiO<sub>2</sub>, a sufficient amount of N was necessary for high-performance products, and the amount of F had a little influence on NH<sub>3</sub> decomposition ratio, and there was an optimal value for Fe element doping, which was 0.06 at% among the prepared samples, and the effect of calcination temperature on NH<sub>3</sub> decomposition under visible light was weak.
2. The NH<sub>3</sub> decomposition ratio of the tri-doped sample under UV light irradiation is still higher than 51.3 %, decreased by 0.8 % after three cycles. The NH<sub>3</sub> decomposition ratio of the tri-doped sample under visible light irradiation is still

- higher than 26.9 %, decreased by 0.4 % after three cycles. Therefore, the reusability of the tri-doped TiO<sub>2</sub> sample after three cycles under UV and visible light irradiation is very good.
3. XRD patterns and SEM and HRTEM images indicated that the tri-doped sample was nanometric anatase with a small amount of rutile with an average particle size of 18 nm. Tri-doping with N, F and Fe inhibited grain growth of TiO<sub>2</sub>, and, thus, suppressed the phase transition from anatase to rutile, and also resulted in some more lattice defects.
  4. XPS analysis showed that the doped N and F atoms replaced lattice oxygen atoms into the crystal lattice of TiO<sub>2</sub>, and the doped Fe atom replaced a lattice Ti atom in the crystal lattice of TiO<sub>2</sub>.
  5. The results of UV–Vis absorption spectra demonstrated that undoped TiO<sub>2</sub> samples had no response to visible light. The tri-doping of 4 at% N, 9 at% F and 0.03 at% Fe within TiO<sub>2</sub> prepared at 600 °C extended the optical absorbing edge of TiO<sub>2</sub> up to 640 nm. The tri-doping of N, F and Fe not only broadened the light response range of TiO<sub>2</sub> to the visible light region, but also improved the absorption performance in the UV light region.
  6. DOS results showed that Fe 3d and N 2p orbits narrowed the band gap of TiO<sub>2</sub>, and F 2p orbit broadened the upper valence bands. The cooperation of N, F and Fe elements enhanced both the light response performance of TiO<sub>2</sub> under UV and visible light, which was consistent with results of the UV–Vis absorption spectra analysis. The tri-doping of N, F and Fe within TiO<sub>2</sub> was a good way to improve the light response performance of TiO<sub>2</sub>.
  7. EDD results showed that under synergistic action of the electron density around N, F and Fe in tri-doped TiO<sub>2</sub>, its photochemical stability and reusability are better than undoped and single-doped TiO<sub>2</sub>.

**Acknowledgments** The financial supports from the National Natural Science Foundation of China (50576071) and Science and Technology Department of Shaanxi Province of China (2013k09-24) are gratefully acknowledged.

## References

1. J. Zhao, X.D. Yang, *Build. Environ.* **38**, 645 (2003)
2. M. Sung, S. Kato, F. Kawanami, M. Sudo, *Build. Environ.* **45**, 2002 (2010)
3. M.Z. Guo, T.C. Ling, C.S. Poon, *Build. Environ.* **53**, 1 (2012)
4. K. Demeestere, J. Dewulf, B.D. Witte, A. Beeldens, H.V. Langenhove, *Build. Environ.* **43**, 406 (2008)
5. A.M. Ramirez, K. Demeestere, N.D. Belie, T. Mäntylä, E. Levänen, *Build. Environ.* **45**, 832 (2010)
6. R. Asahi, T. Morikawa, T. Ohwaki, K. Aoki, Y. Taga, *Science* **293**, 269 (2001)
7. C. Di Valentin, G. Pacchioni, A. Selloni, *Phys. Rev. B* **70**, 085116 (2004)
8. Z.S. Lin, A. Orlov, R.M. Lambert, M.C. Payne, *J. Phys. Chem. B* **109**, 20948 (2005)
9. H. Irie, Y. Watanabe, K. Hashimoto, *J. Phys. Chem. B* **107**, 5483 (2003)
10. D.N. Tafen, J. Wang, N.Q. Wu, J.P. Lewis, *Appl. Phys. Lett.* **94**, 093101 (2009)
11. J.M. Du, G.Y. Zhao, Y.F. Shi, H. Yang, Y.X. Li, G.G. Zhu, Y.J. Mao, R.J. Sa, W.M. Wang, *Appl. Surf. Sci.* **273**, 278 (2013)
12. A. Selvaraj, S. Sivakumar, A.K. Ramasamy, V. Balasubramanian, *Res. Chem. Intermed.* **39**, 2287 (2013)

13. S.U.M. Khan, M. Al-Shahry, W.B.I. Jr, *Science* **297**, 2243 (2002)
14. S.B. Kim, J.Y. Park, C.S. Kim, K. Okuyama, S.E. Lee, H.D. Jang, T.O. Kim, *J. Phys. Chem. C* **119**, 16552 (2015)
15. J.Y. Park, K.H. Lee, B.S. Kim, C.S. Kim, S.E. Lee, K. Okuyama, H.D. Jang, T.O. Kim, *RSC Adv.* **4**, 9946 (2014)
16. B.S. Kim, J.Y. Park, C.S. Kim, S.B. Kim, D.K. Song, H.D. Jang, S.E. Lee, T.O. Kim, *Electrochim. Acta* **174**, 502 (2015)
17. D.V. Wellia, Q.C. Xu, M.A. Sk, K.H. Lim, T.M. Lim, T.T.Y. Tan, *Appl. Catal. A Gen.* **401**, 98 (2011)
18. W.Y. Choi, A. Termin, M.R. Hoffmann, *J. Phys. Chem.* **98**, 13669 (1994)
19. W.P. Huang, X.H. Tang, I. Felner, Y. Kolytyn, A. Gedanken, *Mater. Res. Bull.* **37**, 1721 (2002)
20. F. Lin, D.M. Jiang, X.M. Ma, *J. Alloys Compd.* **470**, 375 (2009)
21. Z.Q. Liu, Y.C. Wang, W. Chu, Z.H. Li, C.C. Ge, *J. Alloys Compd.* **50**, 54 (2010)
22. Y. Liu, C. Xu, Z.D. Feng, *Appl. Surf. Sci.* **314**, 392 (2014)
23. Y.H. Zhang, F.Z. Lv, T. Wu, L. Yu, R. Zhang, B. Shen, X.H. Meng, Z.F. Ye, P.K. Chu, *J. Sol-Gel. Sci. Technol.* **59**, 387 (2011)
24. C.L. Yu, Q. Shu, C.X. Zhang, Z.P. Xie, Q.Z. Fan, *J. Porous Mater.* **19**, 903 (2012)
25. M. Senna, V. Sepelak, J.M. Shi, B. Bauer, A. Feldhoff, V. Laporte, K.D. Becker, *J. Solid State Chem.* **187**, 51 (2012)
26. Z.L. He, W.X. Que, J. Chen, X.T. Yin, Y.C. He, J.B. Ren, A.C.S. *Appl. Mater. Inter.* **4**, 6816 (2012)
27. Y. Lv, Z.P. Fu, B.F. Yang, J. Xu, M. Wu, C.Q. Zhu, Y.X. Zhao, *Mater. Res. Bull.* **46**, 361 (2011)
28. Y.F. Ma, J.L. Zhang, B.Z. Tian, F. Chen, S.Y. Bao, M. Anpo, *Res. Chem. Intermed.* **38**, 1947 (2012)
29. P.L. Zhang, S.Y. Yin, T. Sekino, S.W. Lee, T. Sato, *Res. Chem. Intermed.* **39**, 1509 (2013)
30. F. Yang, H.M. Yang, B.Z. Tian, J.L. Zhang, D.N. He, *Res. Chem. Intermed.* **39**, 1685 (2013)
31. K.J. Duan, Z.M. Liu, J.H. Li, L. Yuan, H. Hu, S.I. Woo, *Catal. Commun.* **57**, 19 (2014)
32. A. Galenda, L. Crociani, N. El Habra, M. Favaro, M.M. Natile, G. Rossetto, *Appl. Surf. Sci.* **314**, 919 (2014)
33. H.B. Song, G.W. Zhou, C.F. Wang, X.J. Jiang, C.C. Wu, T.D. Li, *Res. Chem. Intermed.* **39**, 747 (2013)
34. A.A. Ashkarran, H. Hamidinezhad, H. Haddadi, M. Mahmoudi, *Appl. Surf. Sci.* **301**, 338 (2014)
35. L.C. Jia, C.C. Wu, S. Han, N. Yao, Y.Y. Li, Z.B. Li, B. Chi, J. Pu, L. Jian, *J. Alloys Compd.* **509**, 6067 (2011)
36. Y.F. Zhang, Y.H. Liu, *Res. Chem. Intermed.* (2015). doi:[10.1007/s11164-015-2050-1](https://doi.org/10.1007/s11164-015-2050-1)
37. X.L. Shi, H.B. Qin, X.Y. Yang, Q.X. Zhang, *Mater. Res. Bull.* **47**, 4347 (2012)
38. A. Charanpahari, S.S. Umare, R. Sasikala, *Appl. Surf. Sci.* **282**, 408 (2013)
39. J.K. Burdett, T. Hughbanks, G.J. Miller, J.W. Richardson, J.V. Smith, *J. Am. Chem. Soc.* **109**, 3639 (1987)
40. J.P. Perdew, K. Burke, M. Ernzerhof, *Phys. Rev. Lett.* **77**, 3865 (1996)
41. P.T. He, J. Tao, X.L. Huang, J.J. Xue, *J. Sol-Gel. Sci. Technol.* **68**, 213 (2013)
42. J.H. Cai, Y.J. Ye, J.W. Huang, H.C. Yu, L.N. Ji, *J. Sol-Gel. Sci. Technol.* **62**, 432 (2012)
43. Y.F. Shen, T.X. Xiong, H. Du, H.Z. Jin, J.K. Shang, K. Yang, *J. Sol-Gel. Sci. Technol.* **50**, 98 (2009)
44. Q.C. Xu, D.V. Wellia, M.A. Sk, K.H. Lim, J.S.C. Loo, D.W. Liao, R. Amal, T.T.Y. Tan, *J. Photochem. Photobiol. A* **210**, 181 (2010)
45. T. Yamashita, P. Hayes, *Appl. Surf. Sci.* **254**, 2441 (2008)